THE JOURNAL OF PHYSICAL CHEMISTRY C

ARTICLE

pubs.acs.org/JPCC

Phase Transitions at the Mn/ZnO (000$\bar{1}$) Interface Probed by High Energy X-ray Spectroscopies

Mac C. Mugumaoderha,*[,†] Robert Sporken,[†] Jacques Ghijsen,[†] Frank M.F. de Groot,[‡] and Jacques A. Dumont[†]

[†]Research Centre in Physics of Matter and Radiation, University of Namur (FUNDP), Rue de Bruxelles 61, 5000 Namur, Belgium

[‡]Department of Inorganic Chemistry and Catalysis, Utrecht University, Sorbonnelaan 16, 3584 CA Utrecht, The Netherlands

ABSTRACT: Phase transitions occurring at the Mn/ZnO interface upon annealing are probed in situ by high-energy X-ray: photoelectron and absorption spectroscopies. A thin Mn film (~1 nm) is grown on the (000$\bar{1}$) surface of a ZnO single crystal. Upon annealing to progressively higher temperature ranging from 575 to 800 K, various Mn phases form successively. At first, the Mn film oxidizes and a MnO layer forms on top of the surface. Then, while Mn atoms diffuse deeper into the bulk of ZnO, $Zn_yMn_{3-y}O_4$ starts to form. Finally, at the highest annealing temperature, Mn appears to be substitutionally diluted at Zn sites within the ZnO lattice.

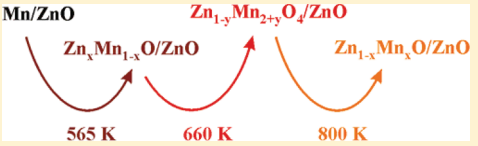

1. INTRODUCTION

The state of a material with a given homogeneous composition at thermodynamical equilibrium depends on its temperature and pressure. At constant pressure, phase transitions will depend only on temperature for such material. When the composition of a material is not uniform as it is in the case for heterostructures, the situation may become more complicated. Indeed, as a result of diffusion processes, concentration gradients will appear near interfaces. Hence, at a given temperature and pressure, the phase observed at a given position in the material will be ruled by the local composition, which also depends on time and on the initial heterojunction stacking sequence. This situation is illustrated in the present article on a relatively simple system, namely, the Mn/ZnO interface. The perfect control of the structure of ZnO-based ternary compounds is indeed very important for achieving the proper physical properties. As an example, a wide diversity of magnetic properties has been reported in the literature for (Zn, TM)O diluted magnetic semiconductors, indicating that the magnetization in such diluted magnetic oxides (DMOs) depends on the growth and doping conditions to a point that the experimental parameters and associated physical properties can hardly be reproduced by different groups.[1−3] The existing literature on the physical chemistry of the Mn/ZnO interface is rather scarce. Zou et al.[4] found that after annealing at high temperature (~900 K) interfacial reactions lead to oxides where Mn is present as Mn^{3+} or Mn^{4+}. The investigations of Guziewicz et al.[5] provided information about the contribution of Mn 3d states to the valence band of ZnMnO.

The phase diagram of the (Zn,Mn)O system is relatively well-known since the mid-60s.[6] For increasing temperatures (between 875 and 1775 K) and for decreasing Mn concentration, Mn appears in a cubic $Zn_yMn_{2-y}O_3$,then in a tetragonal or cubic $Zn_yMn_{3-y}O_4$ spinel, and finally in the zincite (wurtzite) $Zn_{1-z}Mn_zO$ phase. Hence the Mn oxidation state progressively changes from 3+ to 2+ with decreasing concentration or increasing temperature. In the case of thermal diffusion of a thin Mn layer into ZnO, the Mn concentration decreases due to diffusion, while temperature increases. Therefore, the same phase evolution should be expected as for bulk Zn/Mn/O equilibria. Nevertheless, the situation may differ slightly because annealing is performed under ultrahigh vacuum (UHV). The oxygen supply to the Mn therefore requires ZnO decomposition. In a previous paper, we showed that mild annealing of Mn films results in the formation of a thin MnO film, which is unexpected from the phase diagram.[7]

In the present work, we aim at elucidating the phase transition occurring at the interface between Mn and ZnO, especially in relation to the local Mn concentration that is determined by diffusion processes. To achieve this goal, we combined hard X-ray photoelectron spectroscopy (HAXPES) with X-ray absorption near-edge spectroscopy (XANES). As shown in a recent publication by our group,[8] this is a powerful combination of hard X-ray-based techniques for investigating the electronic and structural properties of buried interfaces. In addition, because Mn oxidation can proceed either by the formation of separate oxide phases or by incorporation of Mn atoms at Zn sites, we performed charge transfer multiplet calculations of the Mn 2p X-ray photoelectron spectra to identify the local environment of Mn atoms.

2. EXPERIMENTAL METHODS

The ZnO (000$\bar{1}$) single crystals produced by hydrothermal growth were polished by a mechanical and chemical method (NovaSiC). The samples were then cleaned ex situ in an acetone ultrasonic bath (10 min) and blown dry with nitrogen after the bath.

Next, they were loaded into UHV (base pressure below 2×10^{-9} mbar) at the beamline BW2 at DESY. They were cleaned

Received: July 14, 2011
Revised: November 14, 2011
Published: November 18, 2011

in situ by several Ar^+ sputtering (1 keV, 5 min) and annealing (875 K, 30 min) cycles until no contaminants were seen by HAXPES and a sharp 1 × 1 LEED pattern was observed. The samples were heated by direct current flow across a glassy carbon sample in contact with the single crystal. The temperature was calibrated using a type-K thermocouple in contact with the ZnO surface before UHV cleaning and Mn deposition. Mn was sublimated from a resistively heated filament coiled around a Mn pellet (99.999% purity), with the sample held at room temperature. The deposition rate measured using a quartz oscillator before each Mn deposit ranged between 0.125 and 0.25 nm/min. Mn coverage is specified as equivalent thickness, that is, the thickness of a uniform layer of bulk Mn with the same mass. For HAXPES measurements, a photon energy of 3500 eV was used. Photoelectrons were collected in the normal emission geometry, and Au $4f_{7/2}$ reference spectra were recorded before and after each core level and valence band data set to take into account possible photon energy drifts during the experiments. The intensity of the Au 4f reference spectra was also used to normalize the spectra with respect to photon flux changes occurring during the experiment. XANES measurements were performed by recording the total photon absorption yield (i.e., the drain current) tuning the photon energy around the Mn *K*-edge (6560 eV).

3. THEORETICAL METHODS

For a correct interpretation of the features observed in the Mn 2p spectrum from the annealed Mn/ZnO (000$\bar{1}$) system, we need a proper theoretical description of the photoemission process accounting for interatomic and intra-atomic Coulomb and exchange interactions. Calculations of the theoretical Mn 2p photoelectron spectra from Mn^{2+} were performed using the CTM4XAS code (version 3.1).[9,10] This program is based on the Anderson model of charge-transfer multiplets and provides simulations of X-ray absorption, photoelectron, and X-ray emission spectra of transition-metal compounds. In such compounds, the photoemission of a core electron from the transition-metal atom is often accompanied by an electron transfer from the neighboring O atoms, thus improving the screening of the photohole. Depending on the number of electrons transferred to the Mn atom, several final states may exist leading to the so-called charge-transfer multiplet structures. CTM4XAS includes both the cd^5 and $cd^6\underline{L}$ configurations where *c* denotes the core hole, d^n is the number *n* of electrons on the 3d shell, and $\underline{L}$ is the hole on the ligand 2p orbital after electron transfer. In the calculations, different parameters are modified and adjusted for proper simulation of the experimental data. 10*Dq*, the crystal field splitting, takes positive (respectively negative) values for octahedral (respectively tetrahedral) symmetry. Δ is the charge-transfer parameter, U_{dd} is the d-d Coulomb repulsion energy, U_{pd} is the core hole potential, and T_σ (respectively T_π) is the hybridization energy between the metal d_{xy}, d_{yz}, or d_{zx} (respectively, $d(3z^2\text{-}r^2)$ or $d(x^2\text{-}y^2)$) and the ligand p orbitals. Note that in tetrahedral symmetry calculation, the values of T_σ and T_π used for octahedral symmetry are exchanged. It is also possible to take into account the pd Slater−Condon (ref 9 and refs therein) and 3d- and 2p-spin−orbit coupling parameters (respectively, noted as so3d and so2p). The calculated spectra were convoluted with a 0.2 to 0.3 eV wide (fwhm) Lorentzian function to take into account the finite lifetime of the photohole as well as with a 0.2 to 0.3 eV wide (fwhm) Gaussian function to take into account the limited resolution of the experimental setup. The temperature at which the crystal is analyzed experimentally (∼300 K) is also included in the calculations through a Boltzmann distribution of the occupation of the initial states.

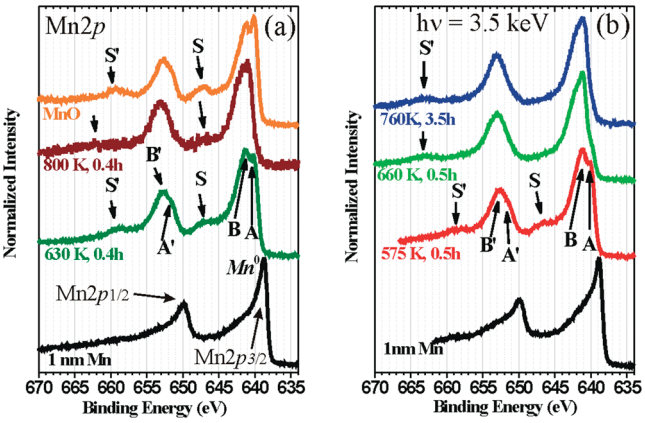

Figure 1. Mn 2p photoelectron spectra recorded at different steps of the experiment (a) on first sample: ∼1 nm Mn on ZnO (000$\bar{1}$) annealed at 630 and 800 K and (b) on second sample: ∼1 nm Mn on ZnO (000$\bar{1}$) annealed at 575, 660, and 760 K from bottom to top. The upper curve in panel a corresponds to a MnO polycrystalline layer grown on a glassy carbon substrate. Labels are described in the text.

4. RESULTS AND DISCUSSION

4.1. Mn 2p Photoelectron Spectra. In a recent publication,[7] we reported the oxidation and diffusion of a thin Mn film grown on ZnO (000$\bar{1}$) upon annealing at 630 and 800 K. Figure 1a shows the Mn 2p XPS spectra obtained from this experiment as well as that from a polycrystalline (rocksalt) MnO thin film. The spin orbit splitting and satellite (S and S′) distance with respect to the main lines clearly indicate that annealing leads to the formation of Mn in a 2+ oxidation state. The most striking observation is that major differences in the fine structure of the main lines (in particular, the intensity ratio between structures A and B) exist between the spectra obtained at the two annealing temperatures but also in comparison with the spectrum from MnO. This indicates that either the Mn^{2+} phases obtained after annealing are not pure or that changes in the crystal field symmetry around Mn atoms occur.

To elucidate these facts and in particular to clarify the crystallographic structure of Mn^{2+} ions, additional XANES and HAXPES measurements were performed. For this experiment, we also annealed the sample at intermediate temperatures to highlight changes in the chemical environment around Mn ions better. Figure 1b shows Mn 2p spectra obtained at these intermediate temperatures. The evolution of the spectra is similar to that from Figure 1a, but a striking difference is also observed: after annealing at 660 and 760 K, satellite S vanishes and S′ is moved 5 eV further apart from the $2p_{1/2}$ line, which is not observed after annealing at 800 K in Figure 1a.

To identify the various phases that formed upon annealing, Mn 2p spectra from the Mn/ZnO system were compared with spectra from various manganese oxide powders (Figure 2). Differences in the stoichiometry from the various Mn oxides affect the shape of the core level lines, the splitting between the $2p_{3/2}$ and $2p_{1/2}$ lines, and the splitting between the satellites and the main lines. The Mn 2p spectrum obtained after annealing at 575 K is similar to that from MnO (Figure 2a), except for the fine

dx.doi.org/10.1021/jp206705p |*J. Phys. Chem. C* 2012, 116, 665–670

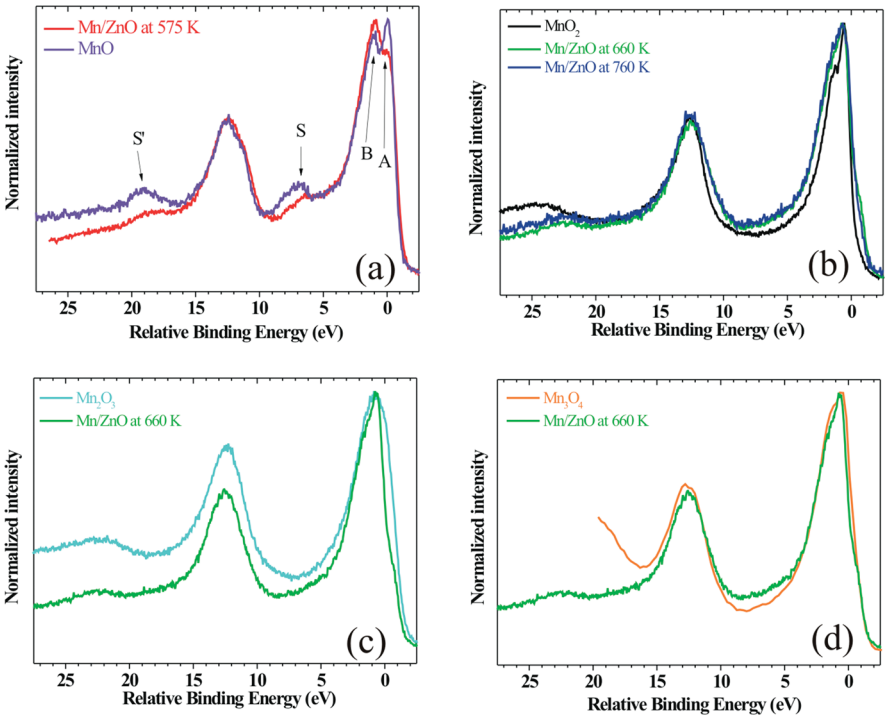

Figure 2. Different Mn 2p spectra: (a) Mn/ZnO annealed at 575 K and polycrystalline rocksalt MnO; (b) Mn/ZnO annealed at 660 K and MnO_2 powder; (c) Mn/ZnO annealed at 660 K and Mn_2O_3 powder; and (d) Mn/ZnO annealed at 660 K and Mn_3O_4 reprinted with the permission from Langell et al.[11] Copyright 1996, American Vacuum Society.

structure of the main lines, but this will be discussed in more detail in a following section. The spectra obtained after annealing at 660 and 760 K are different from the MnO_2 spectrum (Figure 2b) regarding the broadening and the position of the satellite S′. A fair similarity can be observed with those from Mn_2O_3 and Mn_3O_4, especially regarding the spin orbit splitting and the distance of satellite S′. Consequently, XANES analyses were performed to identify the exact phase.

4.2. XANES Analysis. Figure 3a shows XANES measurements from the annealed Mn/ZnO system and the various powders. Qualitatively, the Mn *K*-edge shifts toward higher energies with increasing manganese valence, as for most transition metals.[12−14] The measurements from Figure 3a reveal the same trend as the HAXPES data: the overall shape of the *K*-edge drastically changes after annealing above 660 K. Spectra in Figure 3b confirm that annealing the Mn/ZnO system at 575 K leads to the formation of MnO. After annealing at 660 and 760 K, the XANES spectra become similar to that from Mn_3O_4 (Figure 3c) and not Mn_2O_3.

As previously mentioned, a question is still left open regarding the differences observed (Figure 1) in the fine structure of Mn $2p_{3/2}$ lines from MnO, Mn/ZnO annealed at 575 K (second experiment) or Mn/ZnO annealed at 800 K (first experiment). Additionally the pre-edge feature of the *K*-edge of Mn is also much more intense (inset in Figure 3b) in the case of Mn/ZnO than in polycrystalline MnO. This feature arises from 1s to 3d multipole transitions mediated by the M_n 3d−O 2p covalency. As shown by de Groot et al.,[15] the intensity of the pre-edge feature can be related to the crystal field symmetry around Mn ions: it is, in principle, much more intense in tetrahedral than in octahedral coordination. Manganese ions in MnO are octahedrally coordinated, whereas Mn atoms substituting Zn in ZnO are tetrahedrally coordinated. According to Figure 3b, this implies

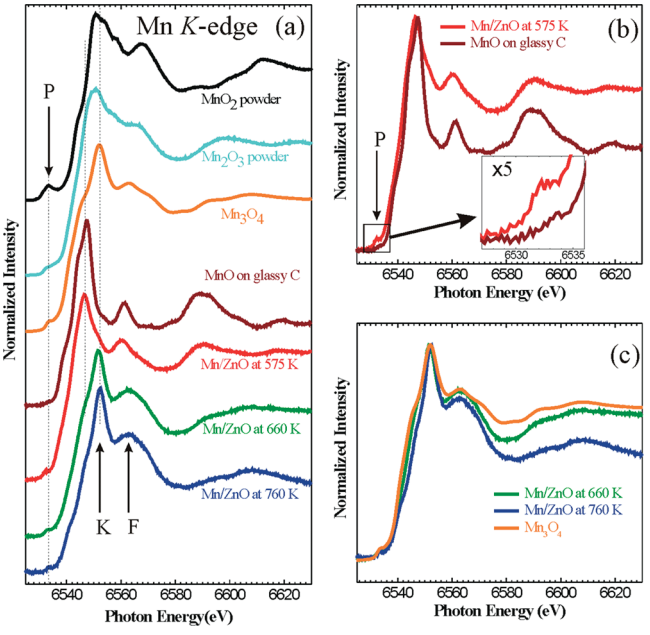

Figure 3. Mn *K*-edge absorption spectra. (a) Stoichiometric manganese oxide powders (data for Mn_3O_4 taken from Droubay et al.[3]), MnO polycrystalline film, and Mn/ZnO annealed at various temperatures; (b) polycrystalline MnO and Mn/ZnO annealed at 575 K; and (c) Mn_3O_4 powder and Mn/ZnO annealed at 660 and 760 K.

that Mn is thermally incorporated into the ZnO wurtzite lattice, where it substitutes Zn.

To verify if such structural differences can explain the fine structure of spectra recorded on Mn/ZnO annealed at 575 or

dx.doi.org/10.1021/jp206705p |J. Phys. Chem. C 2012, 116, 665–670

800 K, we performed charge-transfer multiplet calculations for the Mn 2p spectra from Mn^{2+} in both structures.

4.3. Charge-Transfer Multiplet calculations. The XPS 2p line shape of transition-metal atoms is by nature very complex. The coupling between the 2p core hole and the open 3d valence shell leads to multiplet splitting in photoemission spectra. In the case of transition-metal oxides, multiplet structure may additionally appear due to electron transfer from neighboring oxygen atoms.

The origin of the fine structure observed in the Mn 2p spectra from MnO was for long very controversial.[16−19] The multiplet splitting and intra-atomic valence shell recoupling may play a minor role with respect to the interatomic screening (charge transfer).[10,20] Basically, the XPS 2p spectrum is described assuming the $3d^5 + 3d^6L$ ground state. The main peak is dominated by $2p^53d^6L$, and the satellite is dominated by $2p^53d^5$. Focusing on the $2p_{3/2}$ line, we find that satellite S is presumably originating from 3d electrons recoupling in the same way as expected for atomic Mn. In 2p-ionized Mn atoms, the calculated satellite to the Mn $2p_{3/2}$ multiplet is assigned to 3d recoupled $2p^53d^5(^4P,^4D)4s^2$ states, which corresponds to a final configuration where the spin of one 3d electron has flipped. The multiplet structure (lines A and B in Figures 1 and 2a) in the main $2p_{3/2}$ line can be described in the same manner as in 2p-ionized Mn atom based on a *jj* coupling of the $2p_{3/2}$ hole to the valence shell in its Hund's rule ground state $3d^54s^2(^6S)$. Four multiplet components in the $2p_{3/2}$ peak emerge from this coupling with a total angular momentum $J = 4, 3, 2$, and 1, respectively. A corresponds to $J = 4$ and B corresponds to $J = 3$. Components associated with $J = 2$ and 1 are not resolved in the experimental spectrum.

In conclusion, if charge transfer dominates, then crystal field effects are not well-visible (as in 2p XPS). When atomic effects dominate (2p XAS), crystal field effects are clearly visible. We should thus conclude that the differences observed in our Mn^{2+} spectra are mostly due to the coexistence of various phases. To check this hypothesis and definitively rule out any effect of the crystal field around Mn^{2+} ions, we performed charge-transfer multiplet calculations of the Mn 2p spectra for Mn^{2+} in octahedral (rocksalt MnO) and tetrahedral (wurtzite (Zn,Mn)O) configurations.

Table 1 gives parameters used for calculated spectra shown in Figure 4a,b using CTM4XAS code, which takes charge transfer splitting into account. To simulate our data properly and in light of Bocquet and Fujimori's work,[21] we first tried to match both the intensity ratio and the energy splitting between the main $2p_{3/2}$ line and its charge-transfer satellite by tuning $\Delta(5 \leq \Delta \leq 7$ eV). After this, we worked with fixed $U_{dd}/U_{pd} = 0.83$, 2p and 3d spin−orbit coupling at so2p = 1 (the core spin−orbit coupling is never screened) and so3*d* = 0, according to values found in the literature.[9] Finally, we tuned the value of $10Dq$ ($0 \leq 0Dq \leq 0.0$ eV) and T ($0.53 \leq T_\sigma/T_\pi \leq 0.67$) for the best match between the calculated and experimental spectra. All four components are reproducible by the calculation for $10Dq \leq 0.5$ eV, although some of them are not well-resolved for high values of the Lorentzian and Gaussian broadening parameters. Values of $10Dq$ above 0.5 eV induce other states in the main $2p_{3/2}$ line. Indeed, because of the crystal field the five 3d orbitals loose their degeneracy and become split energy levels: t_{2g} with low energy (localized) and e_g high energy (delocalized) in octahedral symmetry, whereas for tetrahedral symmetry, e has low energy and t_2 has high energy.

As seen in Figure 4a, the experimental spectrum from a polycrystalline (rocksalt) MnO film can be nicely compared with a calculation spectra of Mn^{2+} in an octahedral crystal field. Nevertheless, as shown in Figure 4b, a similar looking spectrum can be obtained using a different parameter set and, more importantly, for a tetrahedral symmetry. In addition, this calculated spectrum matches also quite well those recorded on the Mn/ZnO system annealed at 630 K, which means that the crystal field plays a minor role in the shape of the Mn^{2+} XPS spectra. Nonetheless, it is worth noticing that no calculation of Mn^{2+} in either octahedral or tetrahedral symmetries allowed us to reproduce the relative weights observed for peaks A and B in the Mn $2p_{3/2}$ line of Mn/ZnO annealed at 630 K.

4.4. Phase Transitions in the Mn/ZnO System. Two questions are now left open: (1) What is the origin of the difference in the *A*/*B* intensity ratio observed for MnO and Mn/ZnO annealed up to 630 K? (2) What is the structure of Mn after

Table 1. Best Parameters for Mn 2p Calculation Using CTM4XAS 3.1 Code[a]

symmetry	Δ eV	U_{dd} eV	U_{pd} eV	T_σ eV	T_π eV	so2p	so3d	10Dq eV	Figure
octahedral	6.5	6	7.2	1.9	1	1	1	0	Figure 4a
tetrahedral	5	5	6	1	1.5	1	1	−1	Figure 4b

[a] Parameters used are described in Section 3.

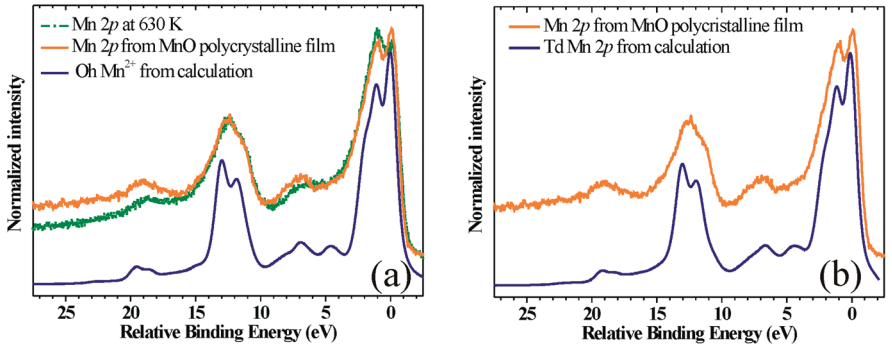

Figure 4. Mn 2p spectra: (a) Mn/ZnO annealed at 630 K and MnO polycrystalline film, both recorded with a photon energy of 3500 eV, and calculated spectrum in octahedral symmetry (using Bocquet's parameter values); (b) MnO polycrystalline film and calculated spectrum assuming tetrahedral symmetry.

dx.doi.org/10.1021/jp206705p |*J. Phys. Chem. C* 2012, 116, 665–670

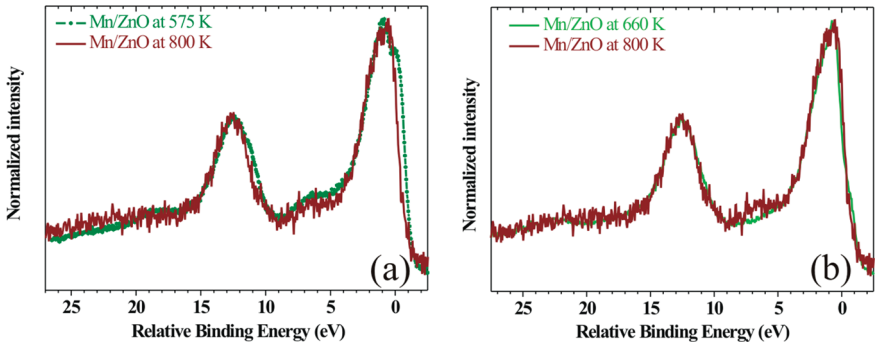

Figure 5. Mn 2p spectra: (a) Mn/ZnO annealed at 575 K compared with that annealed at 800 K and (b) Mn/ZnO annealed at 660 K compared with that annealed at 800 K.

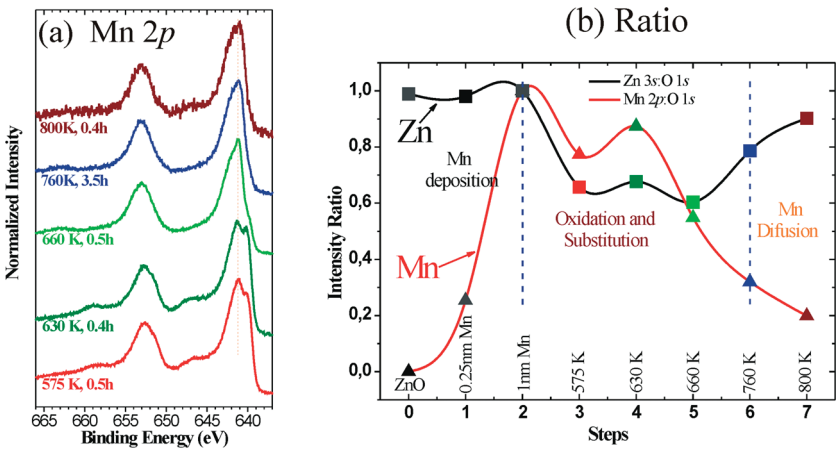

Figure 6. Summary of HAXPES on manganese oxides in ZnO based on annealing temperature. The colors of the symbols used in panel b match those of the corresponding curves in panel a.

annealing at 800 K? The answer to both questions may lie in the presence of an intermediate phase.

As shown in Section 4.2 and above, a wurtzitic (Zn,Mn)O phase is formed after annealing up to 630 K, but a phase transition occurs at 660 K, leading to spectral signatures similar to Mn_3O_4. The usual structure of Mn_3O_4 is hausmannite, corresponding to a cubic oxide phase where one-third of the Mn atoms are tetrahedrally coordinated and in a 2+ oxidation state, and the remaining two-third are octahedrally coordinated in a 3+ oxidation state. According to the literature, $Zn_yMn_{3-y}O_4$ spinel can be formed in wurtzite ZnO, with Mn^{2+} ions substituting Zn atoms and Mn^{3+} being located interstitially in the octahedral cavities.[22] The relative concentration of Mn in both valences is not fixed and, a priori, all phases from pure wurtzitic $Zn_xMn_{1-x}O$ (tetrahedrally coordinated Mn^{2+} ions only) to pure hetaerolite $ZnMn_2O_4$ (octahedrally coordinated Mn^{3+} ions only) are allowed.

To a first approximation, photoemission or photoabsorption spectra from manganese in Mn_3O_4 or $Zn_yMn_{3-y}O_4$ spinel can be considered as a superposition from weighted MnO (Mn^{2+}) and Mn_2O_3 (Mn^{3+}) spectra. After mild annealing (up to 630 K), the Mn 2p photoelectron spectrum (Figures 1a and 2a) is similar to the one from rocksalt MnO, except that the *A*/*B* intensity ratio is larger in the case of MnO. This difference may be explained as a result from minute amounts of octahedrally coordinated Mn^{3+} interstitials.[23−25] Annealing at 660 and 760 K further decreases the intensity of feature *A* to a point where the spectrum becomes similar to that from Mn_3O_4 (as highlighted in Figure 2d)

Finally, annealing at 800 K leads to the presence of a weak satellite S and a weak and broad satellite S′. Our preliminary conclusion is that MnO is the dominant phase in that stage. Figure 5a (respectively b) shows a comparison of the spectrum obtained after annealing at 800 K and Zn/MnO annealed at 575 K (respectively 660 K) and typical from wurtzite $Zn_xMn_{1-x}O$ (respectively $ZnMn_2O_4$). Indeed S is weaker (respectively stronger) than in the case of $Zn_xMn_{1-x}O$ (respectively $ZnMn_2O_4$) and S′ clearly appears as a superposition of S′($Zn_xMn_{1-x}O$) and S′($ZnMn_2O_4$). The straightforward interpretation from these observations is that annealing at 800 K leads to an increase in the Mn^{2+} concentration with respect to Mn^{3+}. As will be seen in the following section, this phenomenon can be understood in relation to the progressive diffusion of Mn in ZnO.

4.5. Mn Diffusion. Figure 6 shows all Mn 2p XPS spectra recorded during both experiments together with the evolution of the Zn 3s/O 1s and Mn 2p/O 1s core level line intensity ratios. The photoemission cross sections are not known in the present range of photon energy. Therefore, we chose to normalize the intensity of our XPS data in the following way:

- Zn 3s and O 1s intensities were both normalized to 1 for the bare oxide. We simply assume that the sample has a 1:1 stoichiometry prior to deposition. Hence the Zn 3s/O 1s ratio is also 1 for the first point of this graph.

dx.doi.org/10.1021/jp206705p |*J. Phys. Chem. C* 2012, 116, 665–670

- Mn 2p was arbitrarily set to 1 for the 1 nm deposit.

These normalizations have no impact on the interpretation of this graph. Indeed, the ratios on which we focus indicate the relative concentration profile of Zn and Mn with respect to the concentration of O.

As seen from Figure 6a, Mn is first oxidized as Mn^{2+} and remains in the vicinity of the surface, whereas the concentration of Zn decreases. Together with the conclusion from XANES analysis, this indicates that a thin MnO wurtzite layer is formed at the surface by Mn substitution of tetrahedrally coordinated Zn atoms, the Zn excess being sublimated. Further annealing leads to the diffusion of Mn and to a progressive decrease (respectively increase) of the Mn/O (respectively Zn/O) intensity ratios. From Figure 6a, diffusion proceeds, whereas a substantial increase in Mn^{3+} with respect to Mn^{2+} is observed. This can easily be explained by the fact that upon Mn diffusion the total metal concentration (Mn + Zn) near the surface decreases with respect to the O concentration, leading to the formation higher valence oxide. Finally, in agreement with the Zn/Mn/O phase diagram, when the concentration of Mn drops as a result from dilution and diffusion, tetrahedrally coordinated Mn^{2+} ions predominate again and interstitial Mn^{3+} progressively disappears.

5. CONCLUSIONS

The present study reveals the fine details of thermally activated processes at the Mn/ZnO interface. The combination of hard X-ray photoelectron and absorption allows identifying the diffusion mechanism. It clearly appears that depending on the annealing temperature different manganese oxides (Mn^{2+} at 575 K and Mn^{3+} at 660 K) form on the ZnO ($000\bar{1}$) surface. Thermal diffusion of Mn^{2+} ions is the predominant diffusion path until the decrease in the Mn concentration allows the formation of ZnMnO zincite.

From a more general point of view, this work demonstrates the ability of hard X-rays to probe buried interfaces and highlight new perspectives regarding the ability to tune the physical and chemical properties at oxide interfaces thermally.

AUTHOR INFORMATION

Corresponding Author

*E-mail: mugumaom@fundp.ac.be, mugcubaka@gmail.com.

ACKNOWLEDGMENT

We thank C. Moisson (NOVASiC), for the MCP polishing of and providing the ZnO single crystals. We would like to thank Heiko Schulz-Ritter, Sebastian Thiess, and Wolfgang Drube for excellent technical and experimental support at the beamline BW2 at DESY (Deutsches Elektronen-Synchrotron). This work was supported by CERUNA-University of Namur, Belgian National Fund for Scientific Research (F.S.R-FNRS), DESY and the European Commission under contract RII3-CT 2004-506008 (IA-SFS).

REFERENCES

(1) Pan, F.; Song, C.; Liu, X. J.; Yang, Y. C.; Zeng, F. *Mater. Sci. Eng., R* **2008**, *62*, 1–35.

(2) Coey, J. M. D.; Chambers, S. A. *MRS Bull.* **2008**, *33*, 1053–1058.

(3) Droubay, T. C.; Keavney, D. J.; Kaspar, T. C.; Heald, S. M.; Wang, C. M.; Johnson, C. A.; Whitaker, K. M.; Gamelin, D. R.; Chambers, S. A. *Phys. Rev. B* **2009**, *79*, 1–9.

(4) Zou, C. W.; Wu, Y. Y.; Sun, B.; Gao, W.; Xu, P. S. *Surf. Interface Anal.* **2007**, *39*, 865–870.

(5) Guziewicz, E.; Kopalko, K.; Sadowski, J.; Guziewicz, M.; Golacki, Z.; Kanski, J.; Ilver, L. *Phys. Scr.* **2005**, *T115*, 541–544.

(6) Driessens, F. C. M.; Rieck, G. D. *J. Inorg. Nucl. Chem.* **1966**, *28*, 1593–1600.

(7) Mugumaoderha, M. C.; Sporken, R.; Ghijsen, J.; Dumont, J. A. *J. Phys. Chem. C* **2011**, *115*, 20603–20609.

(8) Dumont, J. A.; Mugumaoderha, M. C.; Ghijsen, J.; Thiess, S.; Drube, W.; Walz, B.; Tolkiehn, M.; Novikov, D.; de Groot, F. M. F.; Sporken, R. *J. Phys. Chem. C* **2011**, *115*, 7411–7418.

(9) Stavitski, E.; de Groot, F. M. F. *Micron* **2010**, *41*, 687–694.

(10) de Groot, F. M. F.; Kotani, A. *Core Level Spectroscopy of Solids*; CRC Press, Taylor & Francis Group: Boca Raton, FL, 2008.

(11) Langell, M. A.; Hutchings, C. W.; Carson, G. A.; Nassir, M. H. *J. Vac. Sci. Technol., A* **1996**, *14*, 1656–1661.

(12) Chalmin, E.; Farges, F.; Brown, G. E., Jr. *Contrib. Mineral. Petrol.* **2009**, *157*, 111–126.

(13) Stueben, B. L.; Cantrelle, B.; Sneddon, J.; Beck, J. N. *Microchem. J.* **2004**, *76*, 113–120.

(14) de Vries, A. H.; Hozoi, L.; Broer, R. *Int. J. Quantum Chem.* **2003**, *91*, 57–61.

(15) de Groot, F. M. F.; Vankó, G.; Glatzel, P. *J. Phys.: Condens. Matter* **2009**, *21*, 1–7.

(16) Wernet, Ph.; Sonntag, B.; Martins, M.; Glatzel, P.; Obst, B.; Zimmermann, P. *Phys. Rev. A* **2001**, *63*, 1–4.

(17) Bagus, P. S.; Broer, R.; de Jong, W. A.; Nieuwpoort, W. C.; Parmigiani, F.; Sangaletti, L. *Phys. Rev. Lett.* **2000**, *84*, 2259–2262.

(18) Bagus, P. S.; Ilton, E. S. *Phys. Rev. B* **2006**, *73*, 1–14.

(19) Martins, M.; Godehusen, K.; Richter, T.; Wolff, T.; Zimmermann, P. *J. Electron Spectrosc. Relat. Phenom.* **2004**, *137−140*, 345–350.

(20) Okada, K.; Kotani, A. *J. Phys. Soc. Jpn.* **1992**, *61*, 4619–4637.

(21) Bocquet, A. E.; Fujimori, A. *J. Electron Spectrosc. Relat. Phenom.* **1996**, *82*, 87–124.

(22) Lee, J. D.; Kim, H. S.; Jeong, S. Y.; Kim, K. H.; Lee, J. J.; Ahn, B. Y.; Kim, S. I.; Park, K.-W.; Shin, Y. W. *J. Korean Phys. Soc.* **2007**, *51*, 1109–1112.

(23) Berkowitz, A. E.; Rodriguez, G. F.; Hong, J. I.; An, K.; Hyeon, T.; Agarwal, N.; Smith, D. J.; Fullerton, E. E. *J. Phys. D: Appl. Phys.* **2008**, *41*, 1–5.

(24) Barakat, N. A. M.; Woo, K.-D.; Ansari, S. G.; Ko, J.-A.; Kanjwal, M. A.; Kim, H. Y. *Appl. Phys. A: Mater. Sci. Process.* **2009**, *95*, 769–776.

(25) Bayer, V.; Podloucky, R.; Franchini, C.; Allegretti, F.; Xu, B.; Parteder, G.; Ramsey, M. G.; Surnev, S.; Netzer, F. P. *Phys. Rev. B* **2007**, *76*, 1–10.